Supplement of Clim. Past, 16, 757–782, 2020
https://doi.org/10.5194/cp-16-757-2020-supplement

Climate of the Past
Open Access
EGU

Supplement of

Cretaceous oceanic anoxic events prolonged by phosphorus cycle feedbacks

Sebastian Beil et al.

Correspondence to: Sebastian Beil (sebastian.beil@ifg.uni-kiel.de) and Wolfgang Kuhnt (wolfgang.kuhnt@ifg.uni-kiel.de)

Supplementary Material S1 - Phosphorus species in marine sediments

A variety of phosphorus species are discriminated including detrital phosphorus (P_{detr}), authigenic phosphorus (P_{auth}), aluminium and iron bound phosphorus ($P_{Al/Fe}$), and organic bound phosphorus (P_{org}). Detrital phosphorus (P_{detr}) is passively transported as fluviatile sediment load and is regarded as not bio-available due to its inert nature. Phosphorus adhesively bound to iron- or aluminium-crusts ($P_{Al/Fe}$) constitutes an important sink for phosphorus in marine sediments. Early diagenetic conversion of ($P_{Al/Fe}$) via biochemical process can convert this pool to authigenic phosphorus (Jarvis et al., 1994). Authigenic phosphorus (P_{auth}) mainly consists of authigenic apatite (calcium-fluor-apatite, CFA) which precipitates during early diagenesis and is typically enriched in organic-rich sediments of coastal upwelling systems (Ruttenberg, 1993). The two main sources for CFA are microbial remineralization of organic material or remobilization (e.g., during changes of the redox environment towards low-oxygen conditions) of phosphorus bound to iron-oxyhydroxides (Jarvis et al., 1994) during "sink switching" (Ruttenberg and Berner, 1993; Ruttenberg, 1993; Slomp et al., 1996a, b). CFA constitutes the main component extracted as CaP with the CONVEX method (Oxmann et al., 2008). In contrast to organic phosphorus or phosphorus bound to Al-/Fe-oxyhydroxides, CFA is a permanent sink for reactive phosphorus (Ruttenberg, 2003).

Supplementary Material S2 - Comparison of XRF-derived Log(Terr/Ca) including and without Fe

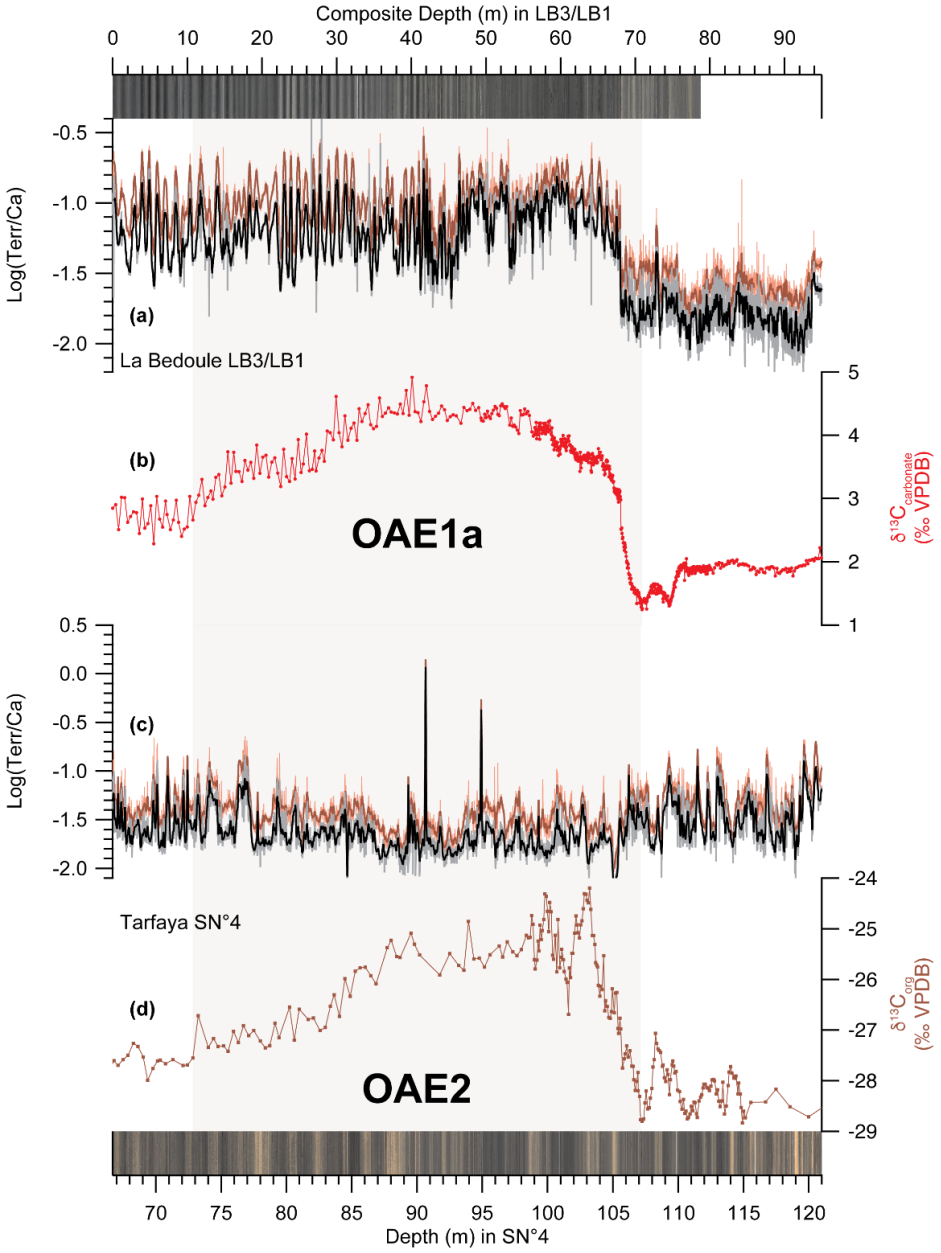

Fig. S2.1. Comparison of XRF-scanning derived Log(Terr/Ca) for OAE1a and OAE2. Log(Terr/Ca) calculated with Fe (red) and without Fe (black). **(a)** Log(Terr/Ca). **(b)** $\delta^{13}C_{carbonate}$ from Lorenzen et al. (2013) for LB1 and from Moullade et al. (2015) for LB3 with new high-resolution isotope data from this study. **(c)** Log(Terr/Ca) from Kuhnt et al. (2017) and Beil et al. (2018). **(d)** $\delta^{13}C_{org}$ for OAE2 from Kuhnt et al. (2017) and Beil et al. (2018). Grey shading marks OAE1a and OAE2.

Supplementary Material S3 - Correlation of NGR record of LB3-LB1 to orbital periodicities for OAE1a

The spliced NGR record of LB3 and LB1 across OAE1a was subdivided into five intervals of relatively consistent orbital periodicities (N1 to N5), based on EHA-analysis (Figs. 4 and S3.1). The uppermost segment N1 extends from 34.22 to 0 m and is characterized by strong cyclicity with wavelengths between 1.5 and 2.5 m and amplitudes predominantly larger than 15 cps. EHA-analysis shows a prominent signal at 1.1 m (0.88 m^{-1}) consistent over the entire interval. A second strong wavelength is detected at 2.2 m (0.45 cycles/m) between 17 and 6 m. The downcore NGR-record of segment N2 between 59.42 and 34.22 m exhibits a decreasing amplitude of short wavelength (0.5 – 2.5 m) cycles from >15 to <10 cps. EHA-analysis reveals a wider range of strong frequencies with the strongest cyclicities detected at wavelengths of 2.5 m (0.4 m^{-1}) and 0.8 m (1.2 m^{-1}). The NGR record of segment N3 from 65.57 to 59.42 m displays 5 cycles with wavelengths between 0.8 and 1.8 m. EHA-analysis is influenced by signals from adjacent segments due to the window size of 6 m, but reveals a high amplitude signal at 1.6 m (0.63 m^{-1}). The NGR curve of segment N4 between 87.32 and 65.57 m shows low amplitude (<7 cps), short wavelength (<1 m) cyclicity overprinted by long wavelength variability (>5 m). A cyclic imprint is detected by EHA-analysis within the wider range of 0.1 to 2.2 m^{-1} with a strong signal with 5.6 m wavelength (0.18 m^{-1}) and weaker signals centred around 0.7 m (1.5 m^{-1}) and 0.5 m (2 m^{-1}). The lowest segment N5 between 105.84 m and 87.32 m shows an extended maximum between 92.67 and 89.17 m with maxima at ~35.5 cps. This interval is otherwise dominated by shorter wavelengths variability (<5 m) with an amplitude of <10 cps. EHA-analysis reveals stronger frequencies in the wavelengths band 1.2 – 7.2 m (0.14 – 0.85 m^{-1}).

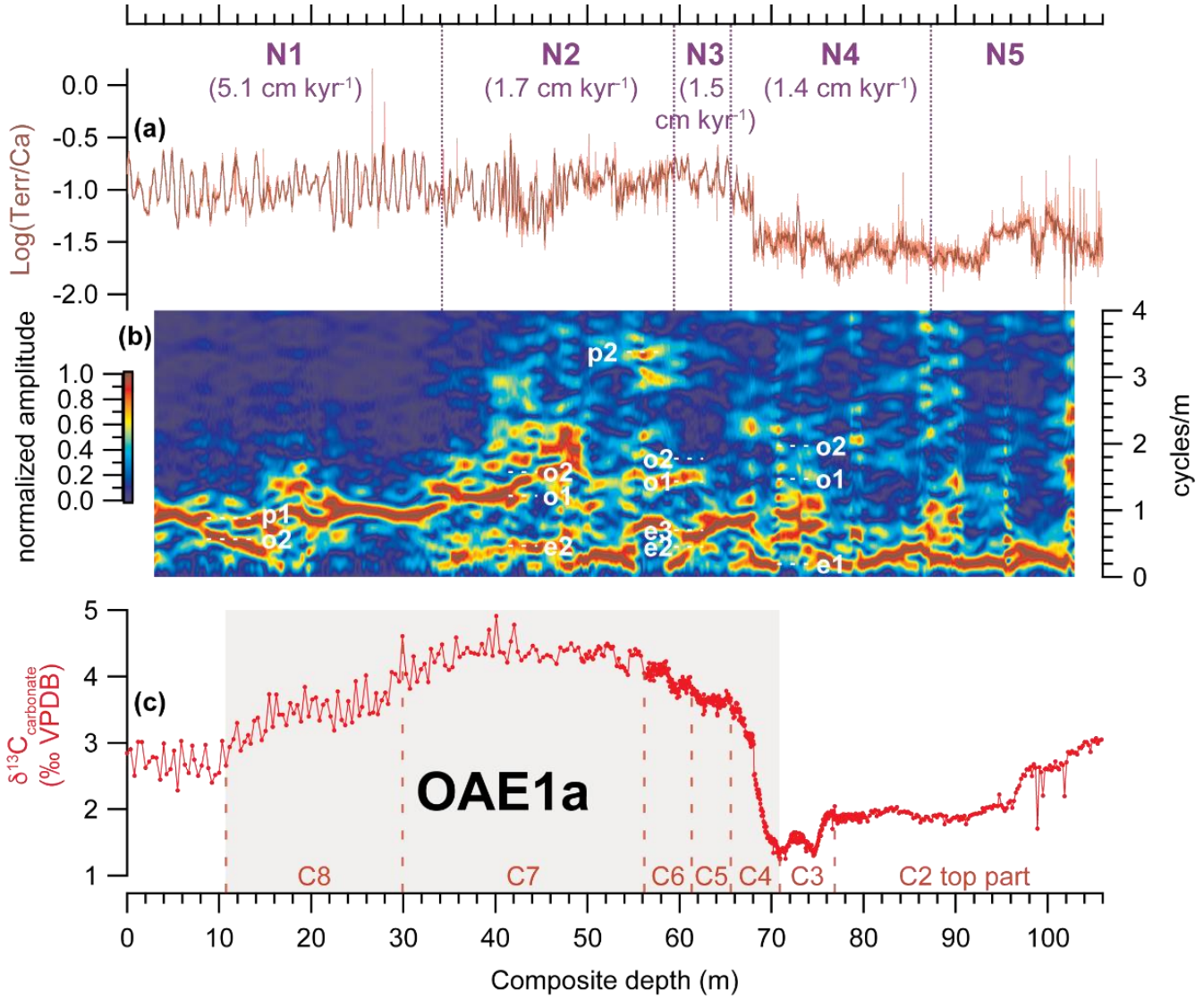

Fig. S3.1. Identification of orbital periodicities over OAE1a from Evolutive Harmonic Analysis (EHA) of XRF-scanning derived Log(Terr/Ca) in Core LB3-LB1. **(a)** Log(Terr/Ca). **(b)** EHA diagram of Log(Terr/Ca); orbital periodicities are indicated by white dashed lines: eccentricity e1 (404 kyr), e2 (124 kyr) and e3 (95 kyr), obliquity o1 (47 kyr) and o2 (37 kyr), precession p1 (22 kyr) and p2 (18 kyr) (Table S8). **(c)** $\delta^{13}C_{carbonate}$ from Lorenzen et al. (2013) for LB1 and from Moullade et al. (2015) for LB3 with new high-resolution isotope data from this study. Purple dashed lines mark boundaries between segments N1-N4 of the NGR record (Supplementary Material S3 and S3.2); mean sedimentation rates in brackets. Carbon isotope stages C2- C8 of Menegatti et al. (1998) are in red with boundaries marked by red dashed lines .

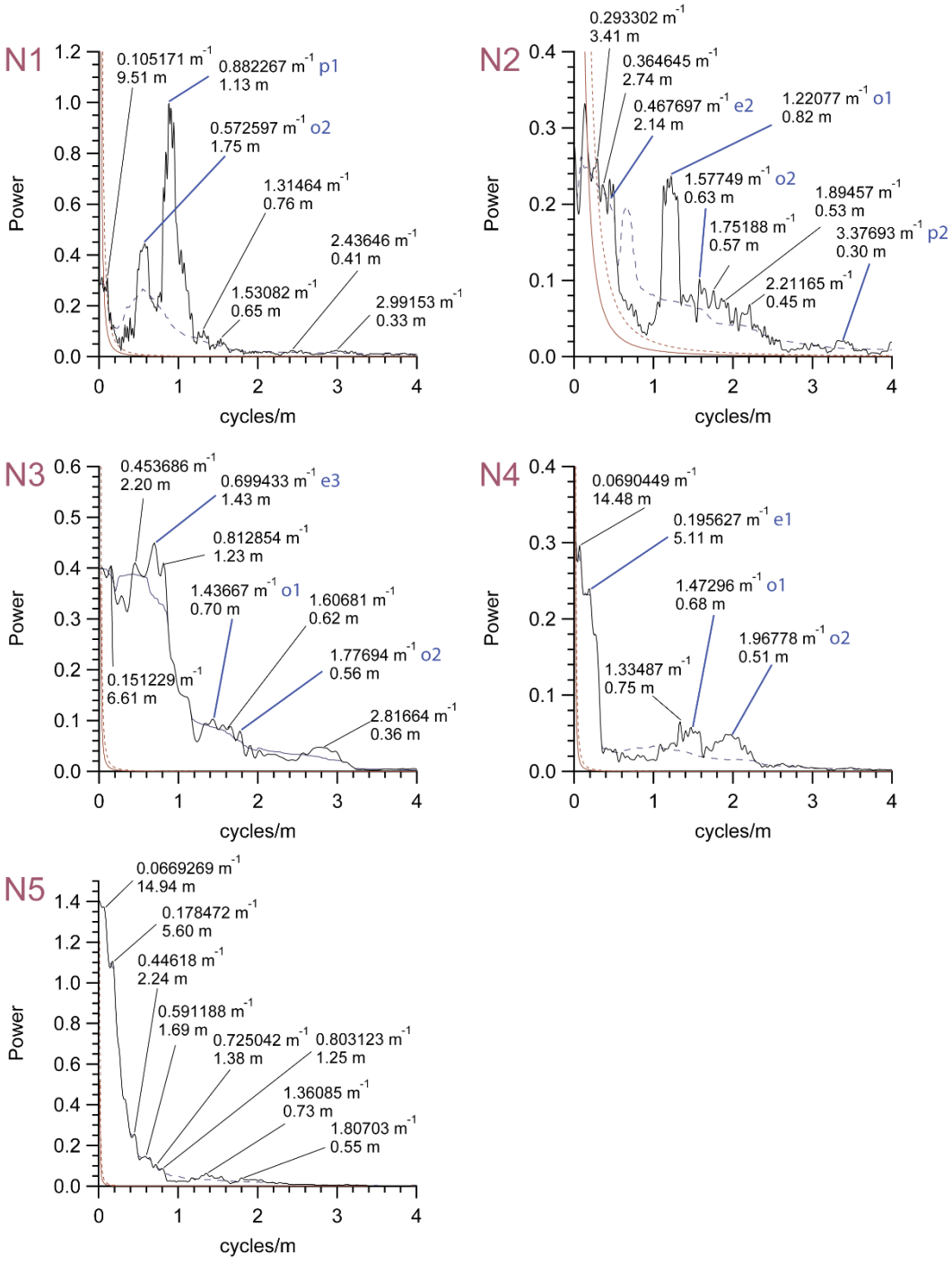

Fig. S3.2. Power spectra of NGR for specific depth segments in La Bédoule Core LB3-LB1: **N1** 0-34.22 m, **N2** 34.22-59.42 m, **N3** 59.42-65.57 m, **N4** 65.57-87.32 m and **N5** 87.32-105.84 m. Red lines indicate red noise level (solid) and 99 % confidence level (dashed). Multitaper method spectral analysis performed with the function *mtm* (Thomson, 1982) of the R-package *astrochron* (Meyers, 2014). Main peaks are marked with frequency and wavelengths and are correlated to orbital frequencies (Supplementary Material S5.1 and S5,2) marked in blue.

Table S3.3. Major frequencies identified in the NGR record of Core LB3-LB1 and correlation to orbital frequencies for the Aptian interval from Laskar et al. (2004, 2011a).

N1			N2			N3			N4		
0-34.22 m			34.22-59.42 m			59.42-65.57 m			65.57-87.32 m		
frequency (m^{-1})	Wavelength (m)	correlated orbital cycle	frequency (m^{-1})	wavelength (m)	correlated orbital cycle	frequency (m^{-1})	wavelength (m)	correlated orbital cycle	frequency (m^{-1})	wavelength (m)	correlated orbital cycle
0.1052	9.51		0.2933	3.41		0.1512	6.61	e1	0.0690	14.48	
0.5726	1.75	(o2)	0.3646	2.74		0.4537	2.20	(e2)	0.1956	5.11	e1
0.8823	1.13	p1	0.4677	2.14	e2	0.6994	1.43	e3	1.3349	0.75	
1.3146	0.76		1.2208	0.82	o1	0.8129	1.23		1.4730	0.68	o1
1.5308	0.65		1.5775	0.63	o2	1.4367	0.70	o1	1.9678	0.51	o2
2.4365	0.41		1.7519	0.57		1.6068	0.62				
2.9915	0.33		1.8946	0.53		1.7769	0.56	o2			
			2.2117	0.45		2.8167	0.36	(p1)			
			3.3769	0.30	p2						
mean sedimentation rate (cm kyr^{-1}):		5.09	mean sedimentation rate (cm kyr^{-1}):		1.74	mean sedimentation rate (cm kyr^{-1}):		1.50	mean sedimentation rate (cm kyr^{-1}):		1.37

Supplementary Material S4 - Correlation of Tarfaya Basin Core SN°4 to Core S13

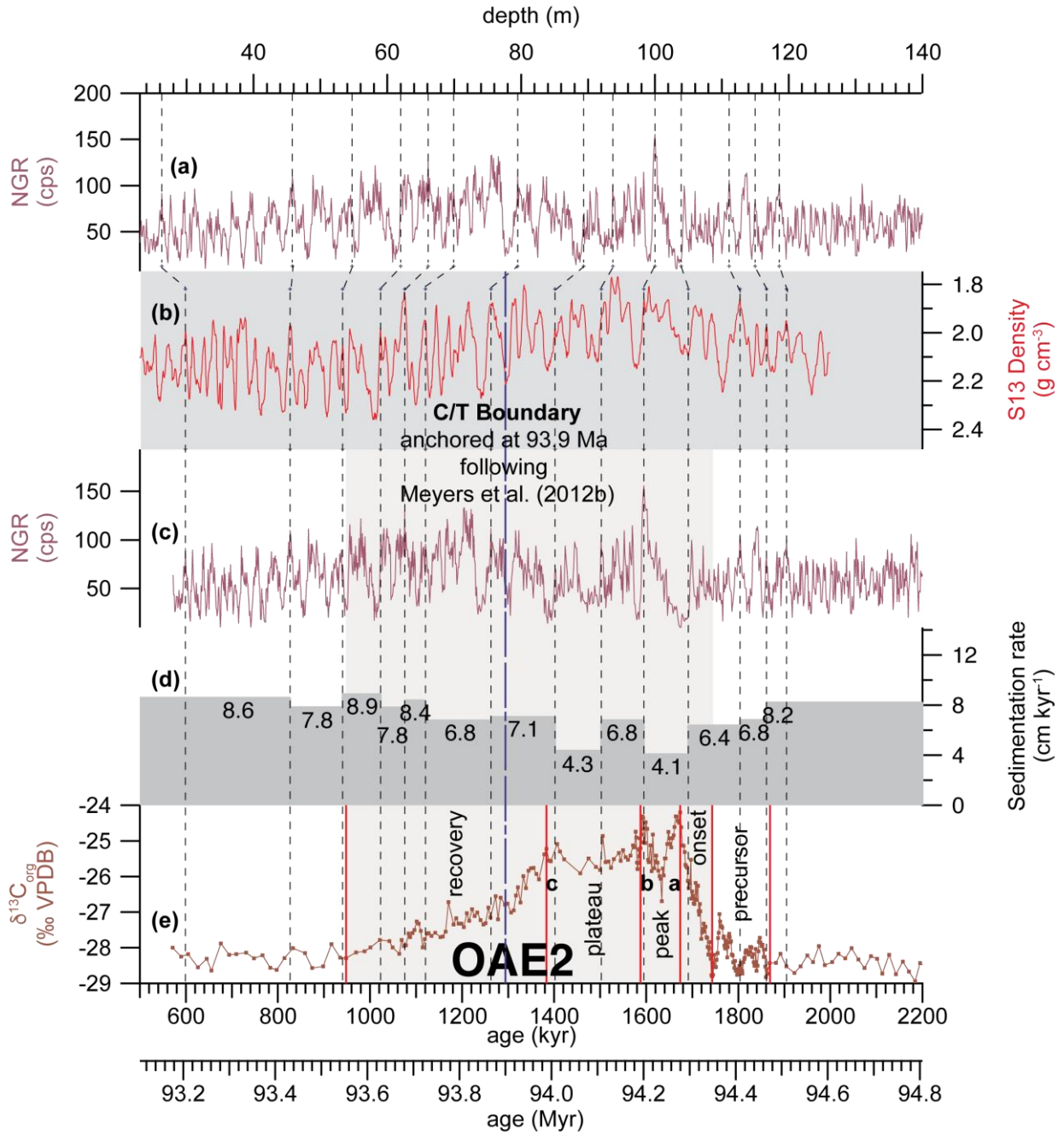

Fig. S4.1. Correlation of Tarfaya Basin Core SN°4 to Core S13. **(a)** NGR record of Core SN°4 on depth scale (top). **(b)** Target density curve from Meyers et al. (2012a) highlighted in light grey. **(c)** NGR record of Core SN°4 on time scale (bottom). **(d)** Sedimentation rates. **(e)** $\delta^{13}C_{org}$; a-c indicates prominent maxima following Voigt et al. (2007). Successive phases of OAE2 indicated by vertical red lines. Vertical, grey, dashed lines indicate tie points; C/T-boundary is marked by blue dashed line. NGR and $\delta^{13}C_{org}$ data are from Kuhnt et al. (2017) and Beil et al. (2018).

Supplementary Material S5 - Aptian and Cenomanian orbital periodicities

Periodicities for precession, obliquity and eccentricity from the orbital solutions La04 (Laskar et al., 2004), La10a-d (Laskar et al., 2011a) and La11 (Laskar et al., 2011b) were calculated by power spectral analysis for the Aptian (113 to 126 Ma, Supplementary Material S5.1 and S5.2) and Cenomanian (93 to 99 Ma, Supplementary Material S5.3 and Beil et al., 2018) intervals. Analysis of the Aptian interval reveals highly significant periodicities (>99 % Confidence level, CL) of 403.76 kyr (long eccentricity e1), 124.29 kyr (short eccentricity e2) and 95.04 kyr (short eccentricity e3) and minor peaks at 131.59 kyr (short eccentricity; e2) and 99.25 kyr (short eccentricity; e3). Highly significant (CL > 99 %) obliquity periodicities are 46.97 (o1) and 36.98 kyr (o2). Precessional periodicities are 22.27 (p1) and 18.03 (p2) kyr.

Main periodicities in the Cenomanian interval are 405.49 kyr (long eccentricity e1), 127.14 kyr (short eccentricity e2) and 96.79 kyr (short eccentricity e3) (Supplementary Material S5.3 and Beil et al., 2018). Three significant periodicities for obliquity are detected with the strongest peak at 37.64 kyr (o2). Weaker periodicities are 48.24 kyr (o1) and 28.07 kyr (o3). A weaker but still significant (CL >99 %) peak is detected at 1.3 Myr, which could reflect the long modulation of obliquity. The strongest precessional peaks are 22.46 kyr (p1), 21.36 kyr (p2) and 18.33 kyr (p3).

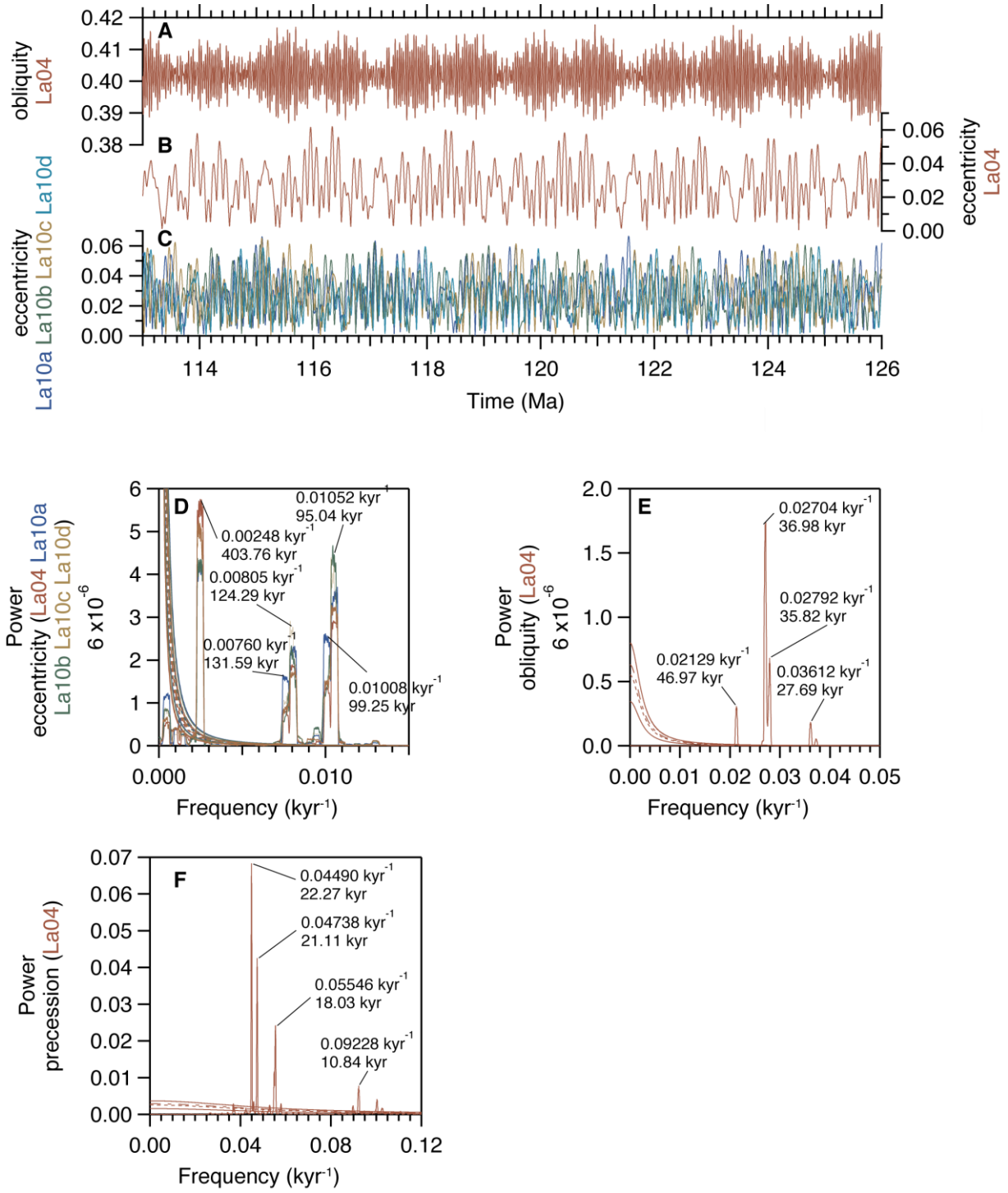

85 **Fig. S5.1.** Orbital solutions for the Aptian interval 113 to 126 Ma from Laskar et al. (2004, 2011a). **(a)** Obliquity from Laskar et al. (2004). **(b)** Eccentricity from Laskar et al. (2004). **(c)** Eccentricity from Laskar et al. (2011a). **(d)** Power spectra for eccentricity from Laskar et al. (2004, 2011a). **(e)** Power spectrum for obliquity from Laskar et al. (2004). **(f)** Power spectrum for precession from Laskar et al. (2004).

Table S5.2. Identified orbital frequencies and ratios of individual frequencies normalized to long eccentricity for the Aptian from Laskar et al. (2004, 2011a).

orbital cycle		frequency (kyr^{-1})	duration (kyr)	ratio (normalized to e1)
eccentricity	e1	0.002477	403.76	1
	e2	0.008045	124.29	3.25
	e3	0.010522	95.04	4.25
obliquity	o1	0.02129	46.97	8.60
	o2	0.027044	36.98	10.92
precession	p1	0.044904	22.27	18.13
	p2	0.055456	18.03	22.39

Table S5.3. Identified orbital frequencies and ratios of individual frequencies normalized to long eccentricity for the Cenomanian from Laskar et al. (2004, 2011a, 2011b).

orbital cycle		frequency (kyr^{-1})	duration (kyr)	ratio (normalized to e1)
eccentricity	e1	0.00246617	405.49	1
	e2	0.00786509	127.14	3.19
	e3	0.0103313	96.79	4.19
obliquity	o1	0.0207292	48.24	8.41
	o2	0.0265614	37.65	10.77
precession	p1	0.0445244	22.46	18.05
	p2	0.0545558	18.33	22.12

Supplementary Material S6 - modified CONVEX extraction method (Oxmann et al., 2008)

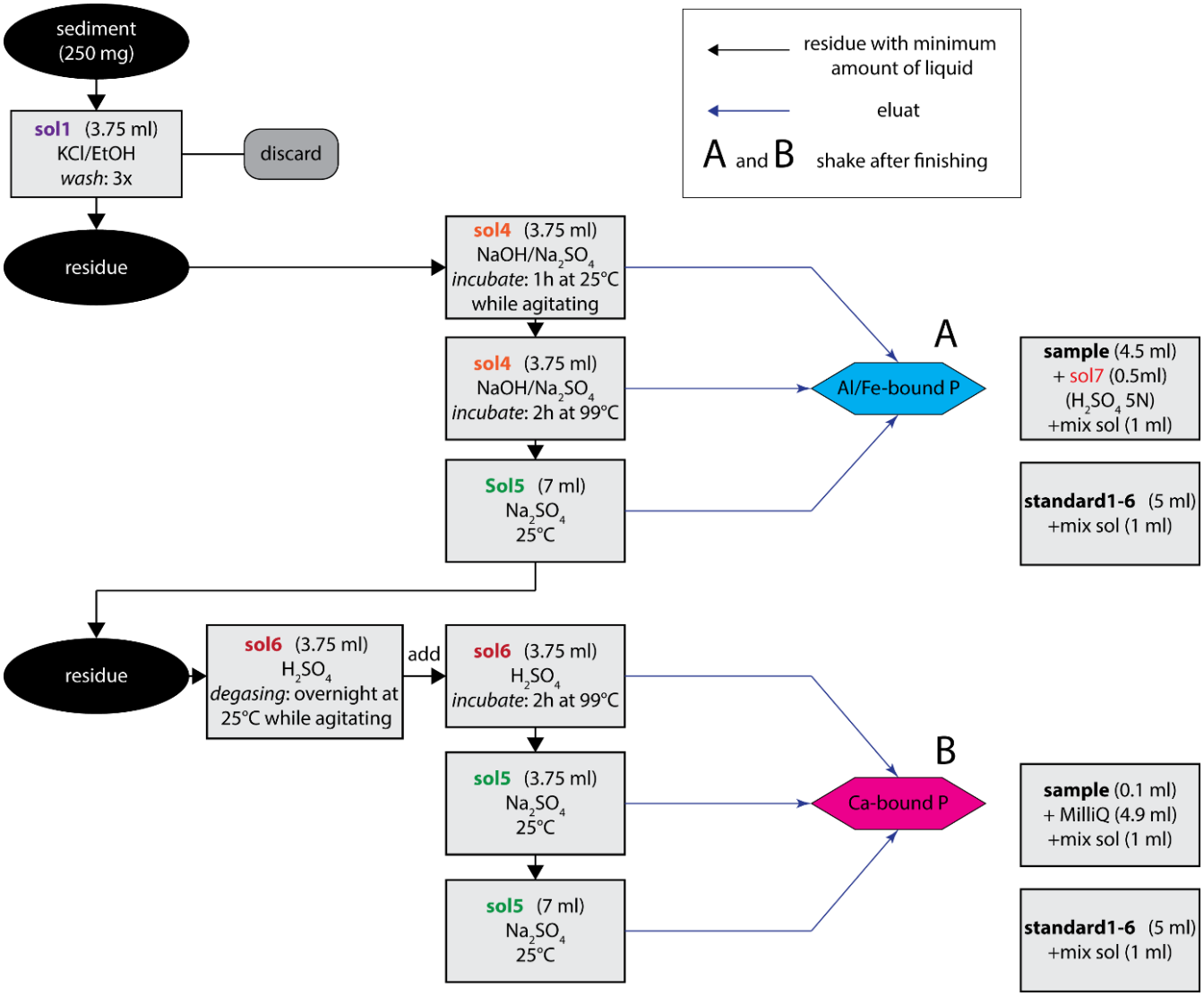

Fig. S6.1. Modified version of the CONVEX extraction method of Oxmann et al. (2008) used for the determination of phosphorus speciation in Core SN°4. Sol1-6 refers to different chemical solutions presented in Supplementary Material S6.2.

Table S6.2 - Chemical solutions for the CONVEX extraction method of Oxmann et al. (2008)

Solution 1 – KCl 1N

Dry KCl at 110°C for 2h

Dissolve dry KCl	in H_2O (MilliQ)	add etilic alcohol
14.912 g	200 ml	300 ml
29.824 g	400 ml	600 ml
37.28 g	500 ml	750 ml

Solution 2 – NaOH 2N

Dissolve NaOH	in H_2O (MilliQ)
8 g	100 ml
40 g	0.5 l
80 g	1 l

Solutions 3 – Na_2SO_4 2N

Dissolve Na_2SO_4	in H_2O (MilliQ)
14.2 g	100 ml
71 g	0.5 l
142 g	1 l

Solution 4 – (Sol2 + Sol3)

NaOH (Sol2)	and	Na_2SO_4 (Sol3)
50%	+	50%

Solution 5 – Na_2SO_4 4%

Dissolve Na_2SO_4	in H_2O (MilliQ)
40 g	1 l
80 g	2 l

Solutions 6 – H_2SO_4 1N

Dilute H_2SO_4	in H_2O (MilliQ)
27 ml	1 l

Solution 7 – H_2SO_4 5N

Dilute H_2SO_4	in H_2O (MilliQ)
135 ml	1 l

Table S6.3 - Photometric solution and standards used for measurement of the phosphorus species extracted with a modified version of the CONVEX extraction scheme of Oxmann et al. (2008)

Mix-solution

1. 4.9N Sulphuric acid
   (1) Ca. 500 ml MilliQ into 1l-flask
   (2) Add 136 ml conc. H_2SO_4 (95-97%) (corrosive!)
   (3) Fill up to 1000 ml MilliQ
2. Ammonium molybdate solution
   (use plastic spatula!)
   (1) Dissolve 10 g ammonium heptamolybdate tetrahydrate (harmful!)
   (2) Fill up to 250 ml with MilliQ
   Solution is stable for 2 weeks.

   Discard if blue colour occurs.
3. Ascorbic acid solutions
   (1) Dissolve 4.5 g L-ascorbin-acid in MilliQ in 250 ml flask
   (2) Fill up to 250 ml with MilliQ
   Solution is stable for 1 week.

   Store cool and in darkness.
4. Potassium antimony tartrate solution
   (1) Dissolve 1.25 g Potassium antimony-(III)-oxitartrate hemihydrate (toxic) in MilliQ in 500 ml flask with magnetic stirrer on heating plate
   (2) Fill up to 500 ml with MilliQ
   Solution is stable for 1 month.

Mixed reagent: **For**	**20 ml**	**40 ml**	**50 ml**	**100 ml**	**120 ml**
4.9N H_2SO_4	10 ml	20 ml	25 ml	50 ml	60 ml
Ammonium molybdate solution	3 ml	6 ml	7.5 ml	15 ml	18 ml
Ascorbic acid solution	6 ml	12 ml	15 ml	30 ml	36 ml
Potassium antimony tartrate solution	1 ml	2 ml	2.5 ml	5 ml	6 ml

Solution is stable for only 12 hours!

Standards

Standard-solution

1. 5 ml Merck standard (1000 mg PO_4/l) into 1l flask
2. Fill up with MilliQ → 5 mg PO_4/l

Standards

Std#	Concentration	Standard-solution	MilliQ	Total Volume
1	0	0 µl	5000 µl	5 ml
2	1%	50 µl	4950 µl	5 ml
3	5%	250 µl	4750 µl	5 ml
4	10%	500 µl	4500 µl	5 ml
5	50%	2500 µl	2500 µl	5 ml
6	75%	3750 µl	1250 µl	5 ml

Add 1 ml mix solution to 5 ml standards or 5 ml samples

Supplementary Material S7 - Phosphorus concentration and speciation across OAE2 and the MCE

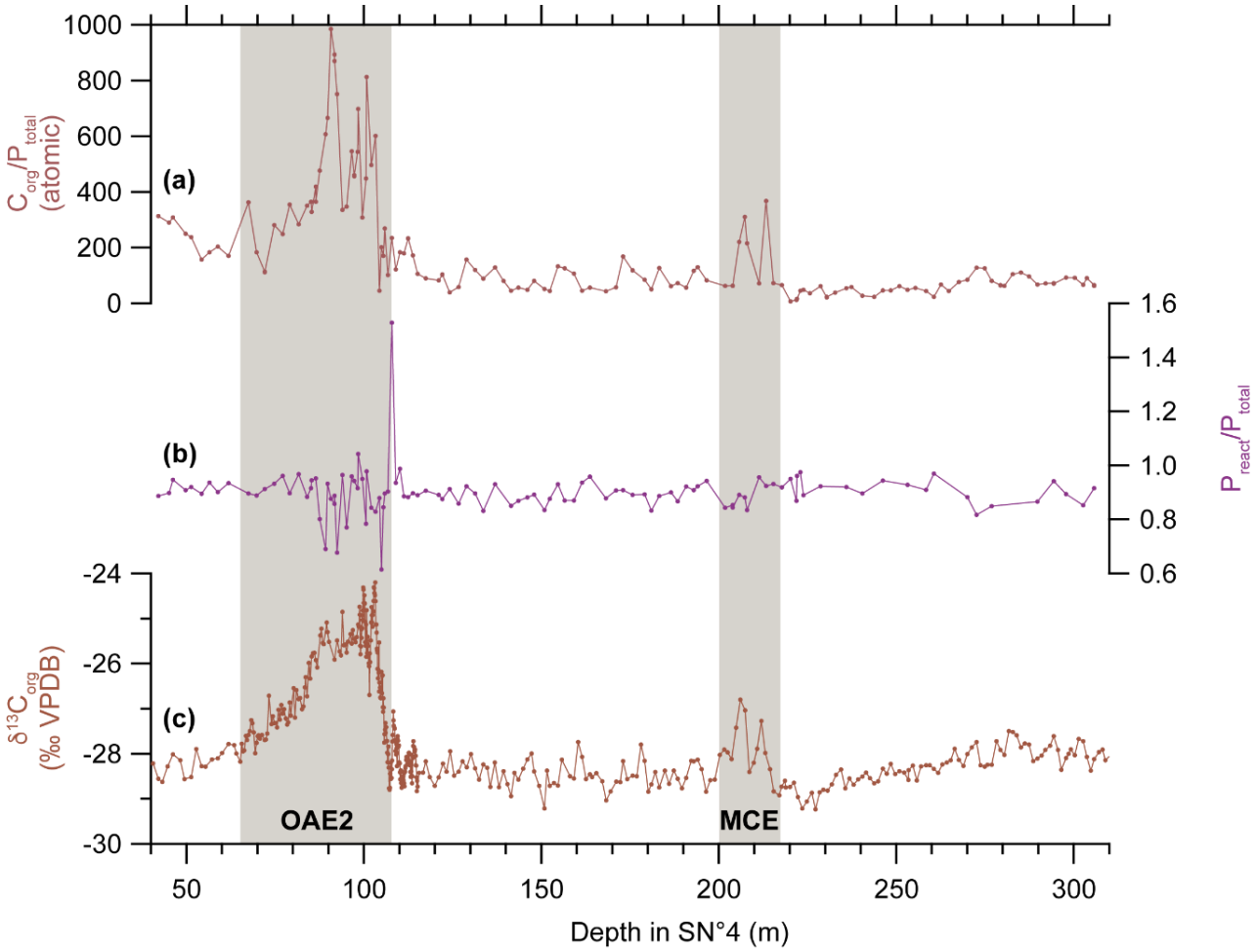

Fig. S7.1. Phosphorus ratios in Tarfaya Basin Core SN°4. **(a)** C_{org}/P_{total}. **(b)** P_{react}/P_{total}. **(c)** $\delta^{13}C_{org}$ from Kuhnt et al. (2017) and Beil et al. (2018).

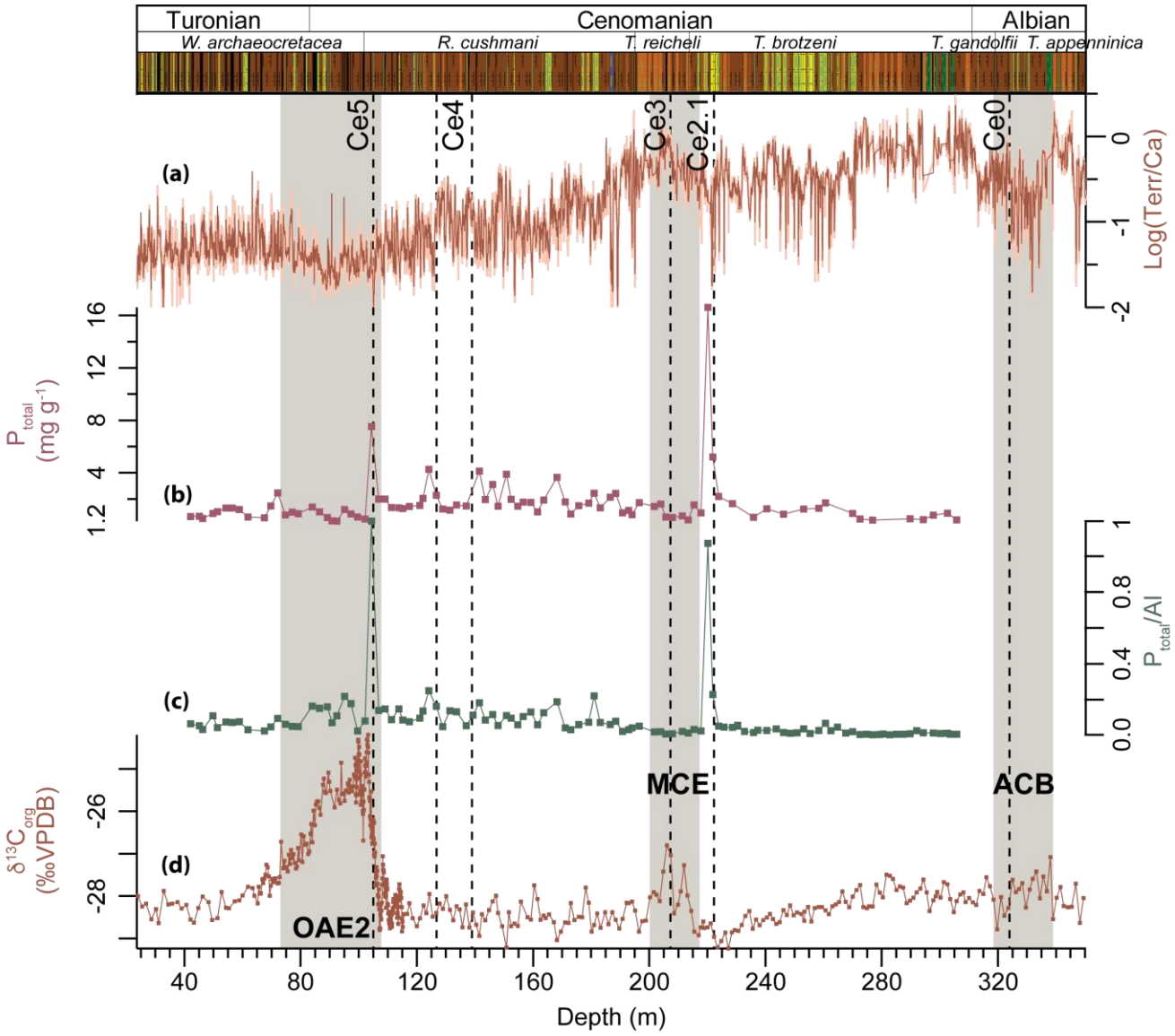

Fig. S7.2. Sea level reconstruction and phosphorus concentrations in Tarfaya Basin Core SN°4. **(a)** XRF-scanning derived Log(Terr/Ca) and regional sea level correlation (Beil et al., 2018; Kuhnt et al., 2009). **(b)** Total phosphorus concentrations (P_{total}) and **(c)** ratio of P_{total} to aluminium. **(d)** $\delta^{13}C_{org}$ from Kuhnt et al. (2017) and Beil et al. (2018). Grey vertical bars indicate Albian-Cenomanian boundary event (ACB), mid-Cenomanian event (MCE) and Oceanic Anoxic Event 2 (OAE2). Vertical dashed lines and abbreviations indicate transgressive surfaces of Cenomanian sea level cycles.

Supplementary Material S8 - Evolution of $\delta^{13}C$ records across OAE2 and OAE1a

The background level of $\delta^{13}C_{org}$ in the Tarfaya Basin Core SN°4 (Fig. 2) is -28.5 ±0.3 ‰ in the interval preceding the precursor phase between 189.65 and 115.57 m. The precursor phase (between 115.57 and 107.14 m) shows two prominent troughs with minima of -28.8 ‰ at 111.46 and 107.14 m, which are preceded by two less pronounced $\delta^{13}C_{org}$ minima at 113.55 and 115.15 m. The onset phase (between 107.14 and 103.22 m) is characterized by a strong increase in $\delta^{13}C_{org}$ of 4.6 ‰ towards the first peak (peak a of Voigt et al., 2007) of $\delta^{13}C_{org}$ with -24.2 ‰ at 103.22 m. The peak phase (between 103.22 and 99.51 m) shows first the decrease towards the intermediate trough with a minimum of -26.7 ‰ at 101.6 m and the second peak (peak b of Voigt et al., 2007) with -24.3 ‰ at 99.80 m. The plateau phase (between 99.51 and 88.03 m) has a mean of -25.4 ±0.3 ‰. During the recovery phase (between 88.03 and 65.2 m) $\delta^{13}C_{org}$ values decrease by 3 ‰. The background level following the end of OAE2 between 65.2 m and the top of the recovered Cretaceous interval at 23.93 m is -28.2 ±0.2 ‰.

A comparable sequence of events is recorded in the $\delta^{13}C_{carbonate}$ dataset of OAE1a in La Bédoule (Fig. 3). The pre-OAE phase between 94.55 m and the top of interval C2 of Menegatti et al. (1998) at 76.87 m has a mean of 1.9 ±0.1 ‰. The precursor phase corresponding to stage C3 of Menegatti et al. (1998) and characterized by two prominent minima in $\delta^{13}C_{carbonate}$ of ~1.3 ‰ is between 76.87 and 70.91 m. The prominent increase of the OAE1a positive isotope excursion, identified as the onset phase, is identical with C4. It begins at the last minimum at 70.91 m and lasts until the first peak of 3.7 ‰ at 65.58 m. This interval is also characterized by a major lithological change at 68.09 m in the composite record of Cores LB1 and LB3 from limestones below to marlstones above (Figs. 3 and Supplementary Material S8.1). This lithological change occurs 4 cm above a major increase in $\delta^{13}C_{carbonate}$ from 2.5 ‰ at 68.09 m to 3.0 ‰ at 68.05 m (Supplementary Material S8.1), suggesting that the lithological change did not influence the increasing trend of $\delta^{13}C_{carbonate}$. The peak phase encompasses C5 and C6 and lasts until the end of the increase to 4.3 ‰ at 55.81 m. The adjacent plateau phase with an average of 4.3 ±0.2 ‰ starts at 55.81 m and lasts until the boundary between C7 and C8 at 29.92 m. The recovery phase between 29.92 and 10.75 m is identical with C8 of Menegatti et al. (1998). The background level of the post-OAE phase for the interval between 10.75 m and the top of the recovered Cretaceous interval is 2.7 ±0.2 ‰.

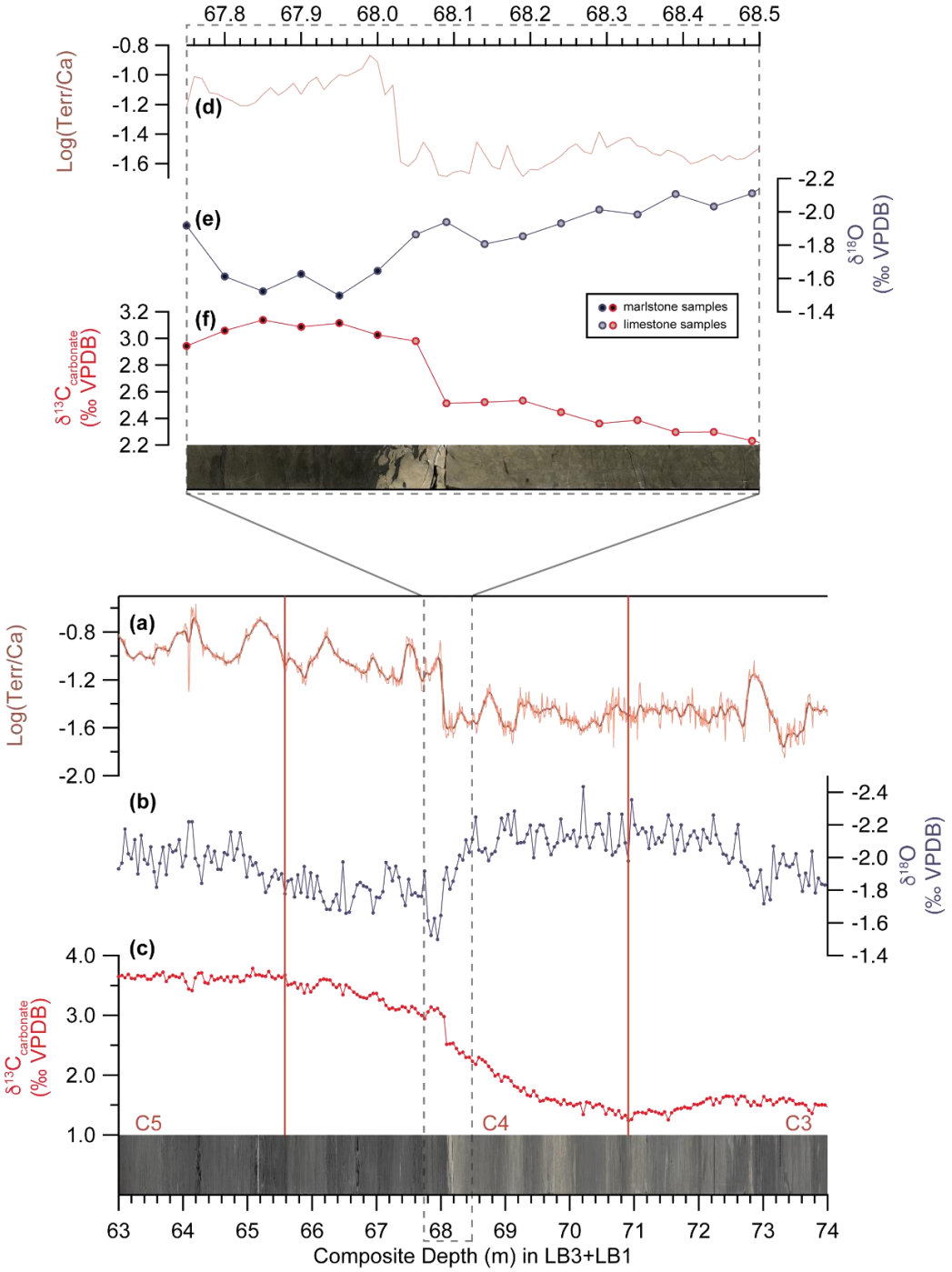

Fig. S8.1. $\delta^{13}C_{carbonate}$ increase during the onset of OAE1a in La Bédoule Core LB1. The interval across the lithological change from dominant limestone to marlstone deposits is shown in higher magnification above. **(a)** and **(d)** Log(Terr/Ca). **(b)** and **(e)** $\delta^{18}O$. **(c)** and **(f)** $\delta^{13}C$. Stable isotope data are from Lorenzen et al. (2013) with new high-resolution isotope data from this study. Carbon isotope stages C3-C5 of Menegatti et al. (1998) are indicated by red lines.

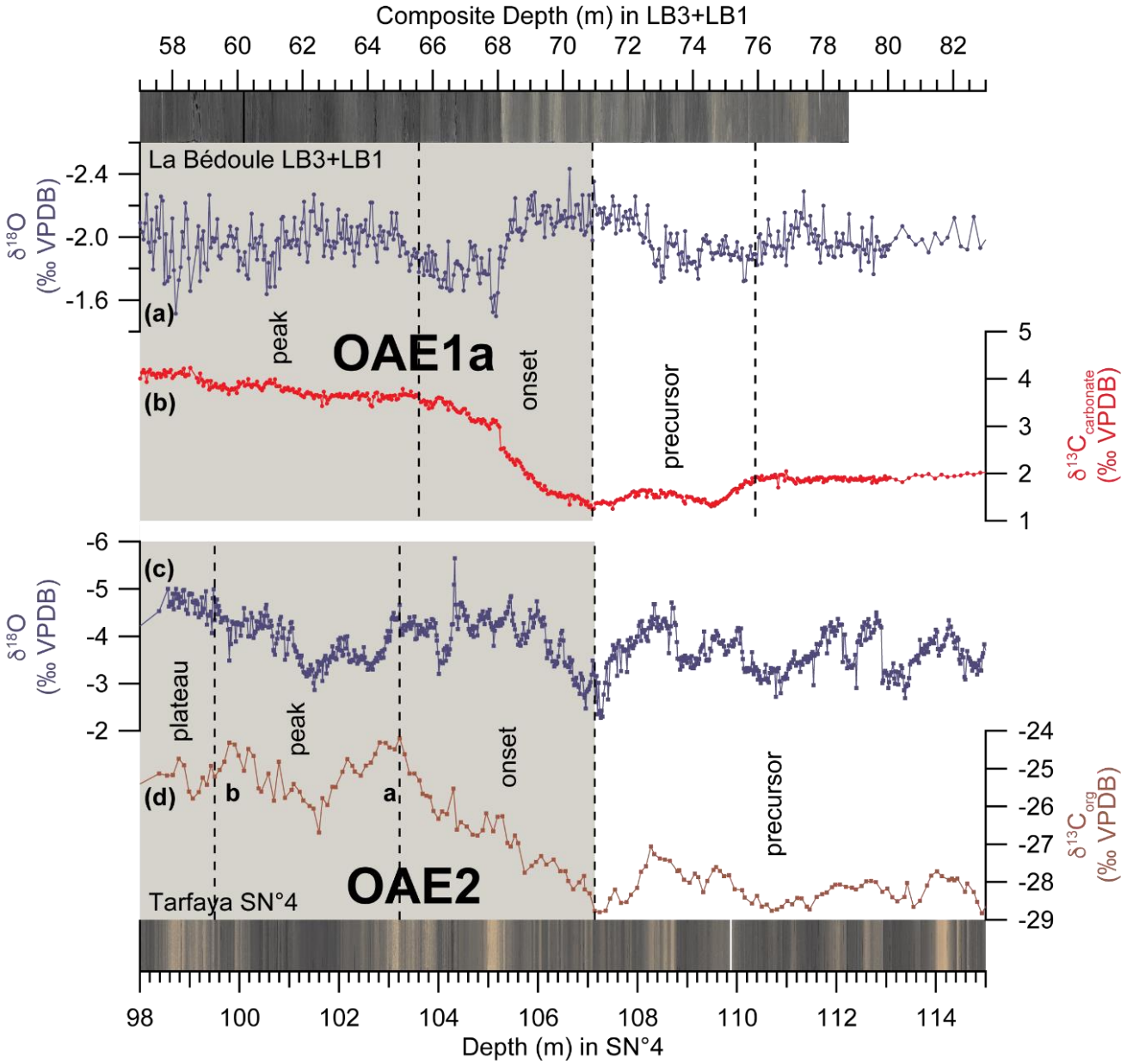

Fig. S9.1. Stable isotope records of La Bédoule CoreLB3-LB1 and Tarfaya Basin Core SN°4 during the early phases of OAE1a and OAE2. **(a)** $\delta^{18}O$ and **(b)** $\delta^{13}C_{carbonate}$ for OAE1a from Lorenzen et al. (2013) with new high-resolution isotope data from this study. **(c)** $\delta^{18}O$ and **(d)** $\delta^{13}C_{org}$ for OAE2 from Kuhnt et al. (2017) and Beil et al. (2018); a-b indicate prominent maxima following Voigt et al. (2007).

Supplementary Material S10 - Redox influence on Al/FeP in Tarfaya Basin Core SN°4

The overall low and nearly constant concentrations of Al/Fe-bound phosphorus in Core SN°4 (Fig. 6) imply either constant anoxic or euxinic conditions causing desorption of phosphorus bound to aluminium- and iron-oxyhydroxides during deposition or early diagenetic conversion of Al/Fe-bound phosphorus into authigenic phosphorus-carbonates. Previous studies proposed that phosphorus burial might be enhanced under ferruginous conditions, implying a negative feedback for the oceanic phosphorus pool and primary production (e.g., März et al., 2008). However, we did not observe a close relationship between Fe and P burial, despite a ferruginous signature in the sediments (Scholz et al., 2019), which supports the notion that dissolved Fe concentrations and rates of Fe oxide precipitation in the Tarfaya Basin were moderate and overall similar to modern upwelling systems (Scholz et al., 2019; Wallmann et al., 2019). The onset of episodic dysoxic to anoxic conditions occurred during the early Cenomanian (above 270 m) in Core SN°4 and consistently oxygen depleted to anoxic environmental conditions prevailed after the MCE (above 185 m), as shown by XRF-scanner Log(Mn/S) (Beil et al., 2018). Increased concentrations of Al/Fe-bound phosphorus below 270 m and a decreased $AlFeP/P_{total}$ ratio (Figs. 6 and 7) support a better oxygenated depositional environment and are therefore in line with these observations. However, low variability in Al/Fe-bound phosphorus and $AlFeP/P_{total}$ between 270 and 185 m, albeit in an interval of low sample spacing (~2.4 m), do not support episodic spread of anoxia in the transition interval between 273 and 185 m (Beil et al., 2018). Concentrations of Ca-bound phosphorus (Fig. 6) decreased slightly with the onset of OAE2 above 103.34 m. These lower concentrations of Al/Fe-bound phosphorus and a stable ratio of Ca- to Al/Fe-bound phosphorus suggest a secondary, syn- or post-depositional conversion of Al/Fe-bound phosphorus into Ca-bound phosphorus.

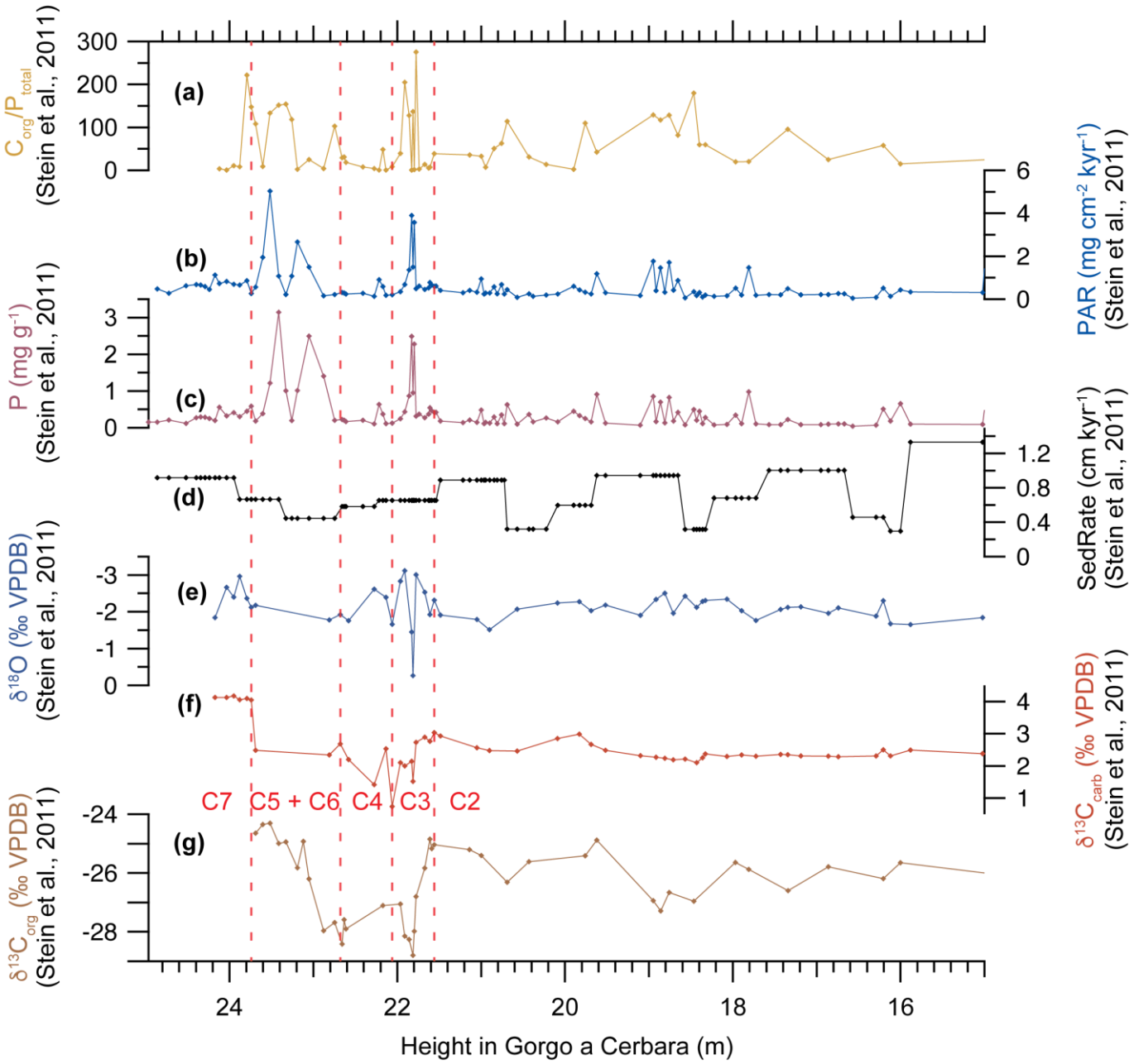

Fig. S11.1. Phosphorus and stable isotope data for the early part of OAE1a from Stein et al. (2011). **(a)** C_{org}/P_{total}. **(b)** Phosphorus accumulation rate (PAR). **(c)** Phosphorus concentration. **(d)** Sedimentation rate (SedRate). **(e)** $\delta^{18}O$. **(f)** $\delta^{13}C_{carb}$. **(g)** $\delta^{13}C_{org}$.

References

Beil, S., Kuhnt, W., Holbourn, A. E., Aquit, M., Flögel, S., Chellai, E. H., and Jabour, H.: New insights into Cenomanian paleoceanography and climate evolution from the Tarfaya Basin, southern Morocco, Cretaceous Res., 84, 451-473, https://doi.org/10.1016/j.cretres.2017.11.006, 2018.

Jarvis, I., Burnett, W. C., Nathan, Y., Almbaydin, F. S. M., Attia, A. K. M., Castro, L. N., Flicoteaux, R., Ezzeldim Hilmy, M., Husain, V., Qutawnah, A. A., Serjani, A., and Zanin, Y. N.: Phosphorite geochemistry: state-of-the-art and environmental concerns, Eclogae Geol. Helv., 87(3), 643-700, 1994.

Kuhnt, W., Holbourn, A., Gale, A., Chellai, E. H., and Kennedy, W. J.: Cenomanian sequence stratigraphy and sea-level fluctuations in the Tarfaya Basin (SW Morocco), Geol. Soc. Am. Bull., 121(11-12), 1695-1710, https://doi.org/10.1130/B26418.1, 2009.

Kuhnt, W., Holbourn, A. E., Beil, S., Aquit, M., Krawczyk, T., Flögel, S., Chellai, E. H., and Jabour, H.: Unraveling the onset of Cretaceous Oceanic Anoxic Event 2 in an extended sediment archive from the Tarfaya-Laayoune Basin, Morocco, Paleoceanography, 32(8), 923-946, https://doi.org/10.1002/2017PA003146, 2017.

Laskar, J., Robutel, P., Joutel, F., Gastineau, M., Correia, A. C. M., and Levrard, B.: A long-term numerical solution for the insolation quantities of the Earth, Astron. Astrophys., 428(1), 261-285, https://doi.org/10.1051/0004-6361:20041335, 2004.

Laskar, J., Fienga, A., Gastineau, M., and Manche, H.: La2010: a new orbital solution for the long-term motion of the Earth, Astron. Astrophys., 532, A89, https://doi.org/10.1051/0004-6361/201116836, 2011a.

Laskar, J., Gastineau, M., Delisle, J. B., Farrés, A., and Fienga, A.: Strong chaos induced by close encounters with Ceres and Vesta, Astron. Astrophys., 532, L4, https://doi.org/10.1051/0004-6361/201117504, 2011b.

Lorenzen, J., Kuhnt, W., Holbourn, A., Flögel, S., Moullade, M., and Tronchetti, G.: A new sediment core from the Bedoulian (Lower Aptian) stratotype at Roquefort-La Bédoule, SE France, Cretaceous Res., 39, 6-16. https://doi.org/10.1016/j.cretres.2012.03.019, 2013.

März, C., Poulton, S. W., Beckmann, B., Küster, K., Wagner, T., and Kasten, S.: Redox sensitivity of P cycling during marine black shale formation: dynamics of sulfidic and anoxic, non-sulfidic bottom waters, Geochim. Cosmochim. Ac., 72(15), 3703-3717, https://doi.org/10.1016/j.gca.2008.04.025, 2008.

Menegatti, A. P., Weissert, H., Brown, R. S., Tyson, R. V., Farrimond, P., Strasser, A., and Caron, M.: High-resolution $\delta^{13}C$ stratigraphy through the early Aptian "Livello Selli" of the Alpine Tethys, Paleoceanography, 13(5), 530-545, https://doi.org/10.1029/98PA01793, 1998.

Meyers, S. R.: Astrochron: An R package for astrochronology, https://cran.r-project.org/package=astrochron, 2014.

Meyers, S. R., Sageman, B. B., and Arthur, M. A.: Obliquity forcing of organic matter accumulation during Oceanic Anoxic Event 2, Paleoceanography, 27(3), PA3212, https://doi.org/10.1029/2012PA002286, 2012a.

Meyers, S. R., Siewert, S. E., Singer, B. S., Sageman, B. B., Condon, D. J., Obradovich, J. D., Jicha, B. R., and Sawyer, D. A.: Intercalibration of radioisotopic and astrochronologic time scales for the Cenomanian-Turonian boundary interval, Western Interior Basin, USA, Geology, 40(1), 7-10, https://doi.org/10.1130/G32261.1, 2012b.

Moullade, M., Tronchetti, G., Granier, B., Bornemann, A., Kuhnt, W., and Lorenzen, J.: High-resolution integrated stratigraphy of the OAE1a and enclosing strata from core drillings in the Bedoulian stratotype (Roquefort-La Bédoule, SE France), Cretaceous Res., 56, 119-140, https://doi.org/10.1016/j.cretres.2015.03.004, 2015.

Oxmann, J. F., Pham, Q. H., and Lara, R. J.: Quantification of individual phosphorus species in sediment: a sequential conversion and extraction method, Eur. J. Soil Sci., 59(6), 1177-1190, https://doi.org/10.1111/j.1365-2389.2008.01062.x, 2008.

Ruttenberg, K. C.: Reassessment of the oceanic residence time of phosphorus, Chem. Geol., 107, 405–409, https://doi.org/10.1016/0009-2541(93)90220-D, 1993.

Ruttenberg, K. C.: The Global Phosphorus Cycle, in: Treatise on Geochemistry (Vol. 8), edited by Turekian, K. K. and Holland, H. D., Elsevier, 585–643, https://doi.org/10.1016/B0-08-043751-6/08153-6, 2003.

Ruttenberg, K. C. and Berner, R. A.: Authigenic apatite formation and burial in sediments from non-upwelling continental margins, Geochim. Cosmochim Ac., 57, 991–1007, https://doi.org/10.1016/0016-7037(93)90035-U, 1993.

Scholz, F., Beil, S., Flögel, S., Lehmann, M. F., Holbourn, A., Wallmann, K., and Kuhnt, W.: Oxygen minimum zone-type biogeochemical cycling in the Cenomanian-Turonian Proto-North Atlantic across Oceanic Anoxic Event 2, Earth Planet. Sc. Lett., 517, 50-60, https://doi.org/10.1016/j.epsl.2019.04.008, 2019.

Slomp C. P., Epping E. H. G., Helder W., and Van Raaphorst W.: A key role for iron-bound phosphorus in authigenic apatite formation in North Atlantic continental platform sediments, J. Mar. Res., 54, 1179–1205, https://doi.org/10.1357/0022240963213745, 1996a.

Slomp, C. P., Van der Gaast, S. J., and Van Raaphorst W.: Phosphorus binding by poorly crystalline iron oxides in North Sea sediments, Mar. Chem., 52, 55–73, https://doi.org/10.1016/0304-4203(95)00078-X, 1996b.

Stein, M., Föllmi, K. B., Westermann, S., Godet, A., Adatte, T., Matera, V., Fleitmann, D., and Berner, Z.: Progressive palaeoenvironmental change during the late Barremian–early Aptian as prelude to Oceanic Anoxic Event 1a: Evidence from the Gorgo a Cerbara section (Umbria-Marche basin, central Italy), Palaeogeogr. Palaeocl., 302(3-4), 396-406, https://doi.org/10.1016/j.palaeo.2011.01.025, 2011.

Thomson, D. J.: Spectrum estimation and harmonic analysis, P. IEEE, 70(9), 1055-1096, https://doi.org/10.1109/PROC.1982.12433, 1982.

Voigt, S., Aurag, A., Leis, F., and Kaplan, U.: Late Cenomanian to Middle Turonian high-resolution carbon isotope stratigraphy: New data from the Münsterland Cretaceous Basin, Germany, Earth Planet. Sc. Lett., 253(1-2), 196-210, https://doi.org/10.1016/j.epsl.2006.10.026, 2007.

Wallmann, K., Flögel, S., Scholz, F., Dale, A. W., Kemena, T. P., Steinig, S., and Kuhnt, W.: Periodic changes in the Cretaceous ocean and climate caused by marine redox see-saw, Nat. Geosci., 12(6), 456, https://doi.org/10.1038/s41561-019-0359-x, 2019.